Study on Correlation between Structural and Electronic Properties of Fluorinated Oligothiophenes Transistors by Controlling Film Thickness

Jui-Fen Chang [1],*, Hua-Shiuan Shie [1], Yaw-Wen Yang [2,3] and Chia-Hsin Wang [2]

1 Department of Optics and Photonics, National Central University, Zhongli 320, Taiwan; m222509443@yahoo.com.tw
2 National Synchrotron Radiation Research Center, Hsinchu 300, Taiwan; yang@nsrrc.org.tw (Y.-W.Y.); wang.ch@nsrrc.org.tw (C.-H.W.)
3 Department of Chemistry, National Tsing-Hua University, Hsinchu 300, Taiwan
* Correspondence: jfchang@dop.ncu.edu.tw; Tel.: +886-3-4227151 (ext. 65263)

Abstract: α,ω-diperfluorohexylquaterthiophene (DFH-4T) has been an attractive n-type material employed in the development of high-mobility organic field-effect transistors. This paper presents a systematic study of the relationship between DFH-4T transistor performance and film structure properties as controlled by deposited thickness. When the DFH-4T thickness increases from 8 nm to 80 nm, the room-temperature field-effect mobility increases monotonically from 0.01 to 1 cm$^2\cdot$V$^{-1}\cdot$s^{-1}, while the threshold voltage shows a different trend of first decrease then increase. The morphology of thin films revealed by atomic force microscopy shows a dramatic change from multilayered terrace to stacked rod like structures as the film thickness is increased. Yet the crystallite structure and the orientation of molecular constituent, as determined by X-ray diffraction and near-edge X-ray absorption fine structure respectively, do not differ much with respect to film thickness increase. Further analyses of low-temperature transport measurements with mobility-edge model demonstrate that the electronic states of DFH-4T transistors are mainly determined by the film continuity and crystallinity of the bottom multilayered terrace. Moreover, the capacitance-voltage measurements of DFH-4T metal-insulator-semiconductor diodes demonstrate a morphological dependence of charge injection from top contacts, which well explains the variation of threshold voltage with thickness. The overall study provides a deeper understanding of microstructural and molecular growth of DFH-4T film and clarify the structural effects on charge transport and injection for implementation of high-mobility top-contact transistors.

Keywords: organic film growth; organic transistor; charge transport and injection mechanisms

1. Introduction

In recent years, extensive studies on chemical synthesis and device engineering of n-type organic semiconductors have significantly increased the material species and electron mobilities approaching the level of p-type counterparts and have broadened the potential applications of organic field-effect transistors (OFETs) in the fields of complementary circuits and light-emitting technologies [1–3]. In addition to the derivatives synthesized based on classic fullerene [4,5], naphthalene diimide [6,7] and perylene diimide [8], many new compounds with high electron mobilities, such as tetraazapentacene-based [9] and dicyanomethylene-substituted thienoquinoidal molecules [10], have been proposed. Perfluorohexyl-substituted oligothiophene is another type of n-type molecule that has attracted much interest due to high mobility, solution processability and high thermal stability and volatility [11]. In particular, α,ω-diperfluorohexyl-quaterthiophene (DFH-4T),

with the highest electron mobility among the DFH-*n*T (*n* = 2–6) series, has been intensively studied in single-component transistors [12,13] and employed as the n-channel material to realize multilayered light-emitting transistors with high ambipolar conductivity and luminescent efficiency [14,15]. Our recent study also demonstrated a high-performance ambipolar OFETs based on a combination of DFH-4T and a p-type molecule, dinaphtho[2,3-*b*:2′,3′-*f*]thieno[3,2-b]thiophene (DNTT), with matched electron and hole mobilities of ~1 cm$^2 \cdot$V$^{-1} \cdot$s^{-1} [16]. Although DFH-4T has great advantages for applications of single- and multi-component transistors, its film structure plays a critical role in determining device performance. Since DFH-4T-based transistors are generally constructed with a bottom-gate configuration, choosing appropriate substrates that support initial film growth with in-plane $\pi-\pi$ intermolecular core interactions and low-density microstructural defects is a prerequisite for achieving high mobility. Previous work by Dholakia et al. has investigated the DFH-4T film growth on Au contact and SiO$_2$ dielectric relevant to bottom-contact transistors [17]. Interestingly, DFH-4T was found to exhibit a unique growth mode on Au surface as driven by strong chemisorption due to interfacial interactions between low-lying π^* orbitals and filled metal d bands. The strong chemisorption at DFH-4T/Au surface and the DFH-4T intermolecular interactions in the bulk film derive a significant transition in molecular orientation and morphology during growth, unlike the fixed molecular orientation as film grows on SiO$_2$. For bottom-contact DFH-4T transistors, the different growth modes on Au contacts and SiO$_2$ dielectric can result in the formation of inhomogeneous microstructures unfavorable for electron injection and therefore mobilities are typically very low (<10^{-4} cm$^2 \cdot$V$^{-1} \cdot$s^{-1}). By contrast, top-contact transistors can yield much higher mobilities and has been commonly adopted in multi-component device applications. When it is necessary to deposit metal contact or even organic semiconductor on top of DFH-4T film, surface morphology is another important feature to be concerned, since it directly affects the quality of heterointerface that determines charge injection from top contacts or transport property of organic semiconductor deposited thereon and can lead to very different OFET function [16]. DFH-4T film morphology depends on manifold factors such as the underlying substrate, deposition conditions and thickness and usually exhibits complex microstructures. In order to optimize the top-contact DFH-4T transistors and broaden their related applications, more detailed studies are needed to understand how the DFH-4T film grows from interface to bulk on a given substrate and which structural factors can essentially influence the transport and injection properties.

Previously, we reported the highest mobility of 2.1 cm$^2 \cdot$V$^{-1} \cdot$s^{-1} for a single-component DFH-4T transistor with the top-contact geometry and suggested that the morphological feature with randomly stacked large-scale rod like crystals is a key attribute for effective charge injection and superior device performance [16]. Behind this complex film morphology, however, how the structure is formed and its effect on the charge transport and injection mechanisms remain unclear. Based on the same processing conditions, here we take a close examination of the structural properties of DFH-4T film with thickness ranging from monolayer to several tens of nanometers and correlate the structure property change with the charge transport and injection characteristics of the top-contact OFET. The paper is organized as follows. The transistor characterizations as a function of DFH-4T thickness is reported in Section 2. In Section 3 we report on the characterization of the thickness-dependent thin film properties such as morphology, microcrystalline state and orientation of molecular constituents by mean of atomic force microscopy (AFM), X-ray diffraction (XRD) and near-edge X-ray absorption fine structure (NEXAFS) measurements, respectively. In Section 4 we perform the low temperature transport measurement and analysis with mobility-edge (ME) model to study the electronic states of DFH-4T OFETs with different thicknesses. This allows us to clarify the microstructural factors that determine the transport property of DFH-4T films. In Section 5 we discuss the morphological effects on the charge injection of DFH-4T OFETs on the basis of capacitance-voltage (C–V) response measurement. A conclusion is given in Section 6.

2. Transistor Characterization

The DFH-4T transistors for this study were fabricated in a bottom-gate, top-contact configuration (Figure 1a). We used a heavily n-doped Si wafer with 300 nm thermally grown SiO_2 as the substrate. After cleaning the substrate, 200 nm thick poly (methyl methacrylate) (PMMA) was spun on the Si/SiO_2 substrate to facilitate the microstructural growth of DFH-4T and provide a good dielectric with few –OH groups that could trap electrons. This yields a total insulator capacitance C_i = 6.4 nF·cm^{-2} for the transistors. The DFH-4T (Lumtec Co) was then deposited onto the substrate at 323 K in high vacuum (<10^{-6} mbar) at a rate of 0.1 Å/s, with the thickness varied from 3 nm to 80 nm. Final thicknesses were monitored by a quartz crystal microbalance during deposition process and calibrated by using AFM after deposition. Hereafter, the film thicknesses are described as the mean thickness value. Finally, the top source/drain electrodes (80 nm Ag) was evaporated on the DFH-4T layer to complete the transistor. The channel length (L) and width (W) were 100 μm and 1500 μm, respectively. All the measurements of I–V characteristics of transistors were carried out in a Janis ST300 cryostat (Janis Research Company, Woburn, MA, USA) at a controlled temperature from 300 K to 80 K with Keysight B1500A semiconductor parameter analyzer (Keysight Technologies, Santa Rosa, CA, USA).
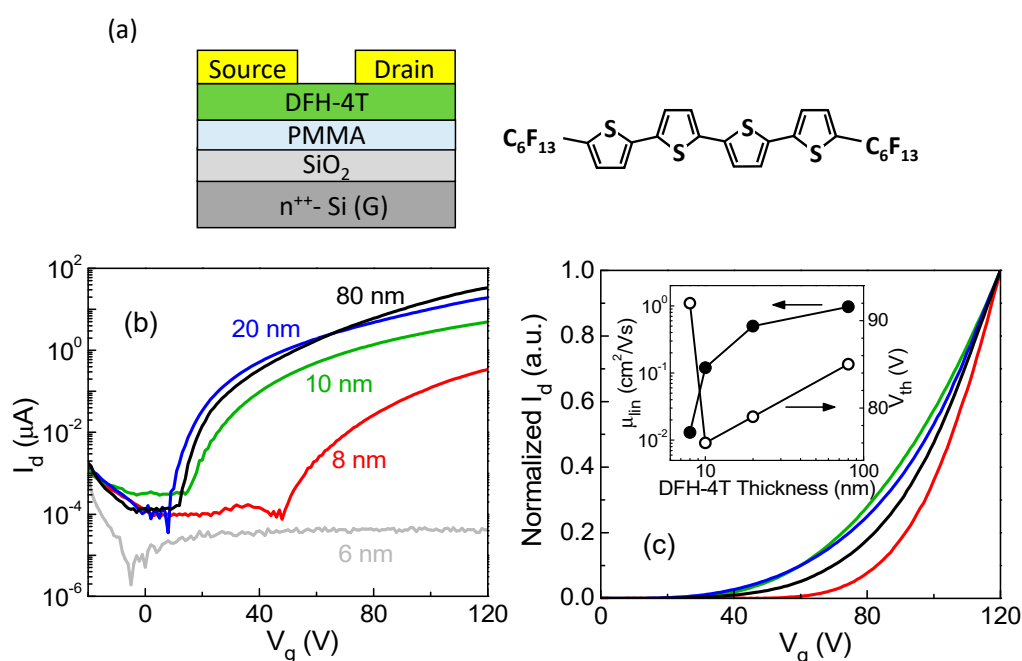

Figure 1. (**a**) Chemical structure of DFH-4T and schematic illustration of the bottom-gate, top-contact DFH-4T organic field effect transistor (OFET). (**b**) Linear transfer characteristics (V_d = 10 V) of DFH-4T transistors with various DFH-4T thicknesses at room temperature (300 K). (**c**) The same transfer characteristics as shown in (**b**) plotted on a linear scale and normalized respectively with the maximum current at V_g = 120 V, revealing different turn-on thresholds of various devices. The inset shows the extracted linear mobility and threshold voltage as a function of DFH-4T thickness.

Figure 1b shows the linear transfer characteristics (V_d = 10 V) of DFH-4T transistors with different thicknesses at room temperature (300 K). No conductive current was detected in the device with 6 nm (and thinner) DFH-4T. The transistor behavior appears when the DFH-4T thickness increases to 8 nm but a high onset voltage V_{on} (~50 V) and low on-current imply the presence of a large number of electronic defect states. For the 10 nm device, V_{on} is significantly reduced to less than 20 V and the on-current is increased by more than one order of magnitude as compared to the 8 nm device. When the thickness exceeds 10 nm, the device shows no apparent shift of V_{on}. The on-current is increased by few folds between 10 nm and 20 nm but only increased a little between 20 nm and 80 nm. Figure 1c shows the same transfer curves normalized respectively with their maximum current at V_g = 120 V,

revealing more clearly the turn-on behavior of different devices. We calculate the linear field-effect mobilities (μ_{lin}) by using a conventional equation

$$\mu_{lin} = \frac{L}{WC_iV_d} \frac{I_d}{(V_g - V_{th})} \tag{1}$$

where V_{th} is the threshold voltage extracted by extrapolating the linear portion of the I_d versus V_g curve to $I_d = 0$. The inset of Figure 1c summarizes how μ_{lin} and V_{th} vary with the DFH-4T thickness. Overall, μ_{lin} increases sharply from 0.01 $cm^2 \cdot V^{-1} \cdot s^{-1}$ to 0.5 $cm^2 \cdot V^{-1} \cdot s^{-1}$ in the range of 8–20 nm and tends to level off above 20 nm, reaching about 1 $cm^2 \cdot V^{-1} \cdot s^{-1}$ at the 80 nm. In contrast, it is interesting to note that V_{th} is highest in the 8 nm device, then decreases abruptly in the 10 nm device and increases again above 10 nm. For OFETs, it is generally expected that V_{th} decreases with the increasing thickness for the first few monolayers due to a reduction of interface trap states and becomes roughly fixed once the film is sufficiently thick due to a stabilization of interface trap density. The nonmonotonic variation of V_{th} in DFH-4T transistors implies some underlying mechanisms that might involve electron injection and accumulation above 10 nm. As will be discussed below, the thickness dependence of DFH-4T transistor characteristics can be well understood from the structural evolution in the film growth.

3. Structural Property Characterization

AFM measurements (Veeco/DI NanoMan D3100CL, EnviroScope AFM in tapping mode) were first performed to shed light on the possible correlation between the transistor performance and the DFH-4T film morphology (Figure 2). In the 3 nm film, it can be seen that the initial growth of the first layer on PMMA exhibits isolated dendrimer microstructures. In the 6 nm film, the first layered dendrimers grow larger but remain isolated, while the second layered terrace structures begin to form. The multilayered terrace structures in the 8 nm film reach a continuum percolation threshold, so that the transistor becomes conductive. However, a prevalent presence of voids and structural defects could be the main cause for a high turn-on threshold and low mobility. It is noted that the measured step heights in the 3–8 nm films are approximately multiples of 3 nm. This corresponds to one-half of the DFH-4T *a*-axis unit cell dimension [17], implying that the long molecular axis is aligned along the surface normal. In the 10 nm film, the multilayered terrace structures cover the surface to a greater extent, which may account for the sharply increased mobility. Interestingly, a low density of large-scale rod like crystals, with a length of 100–1000 nm and a height of ~100 nm, form on top of terrace structures. For even thicker films, the density of rod like crystals is found to increase with thickness and eventually forms a densely packed crystal network in the 80 nm film. The height and diameter of the crystals also increase with thickness (~200 nm in the 80 nm film) but the lengths of the crystals do not increase much. However, the increased density and size of rod like crystals do not well correspond to the mobility variation for the thickness from 10 nm to 80 nm. As seen in the 20 nm film, the crystals are not yet formed into a network and unlikely contribute to the effective current pathways that result in a five-fold increase of mobility for the thickness from 10 nm to 20 nm. And even an interconnected crystal network is formed in the 80 nm film, the mobility shows little enhancement for the thickness between 20 nm and 80 nm. We therefore conjecture that the improved film quality of the bottom multilayered terrace in the 10–80 nm thick films may reflect more on the mobility variation. The surface coverage of the terrace structures could be almost complete in the 20 nm film but not much further improved in the 80 nm film, so that the mobility still increases for the thickness from 10 nm to 20 nm and becomes saturated for the thickness of more than 20 nm.
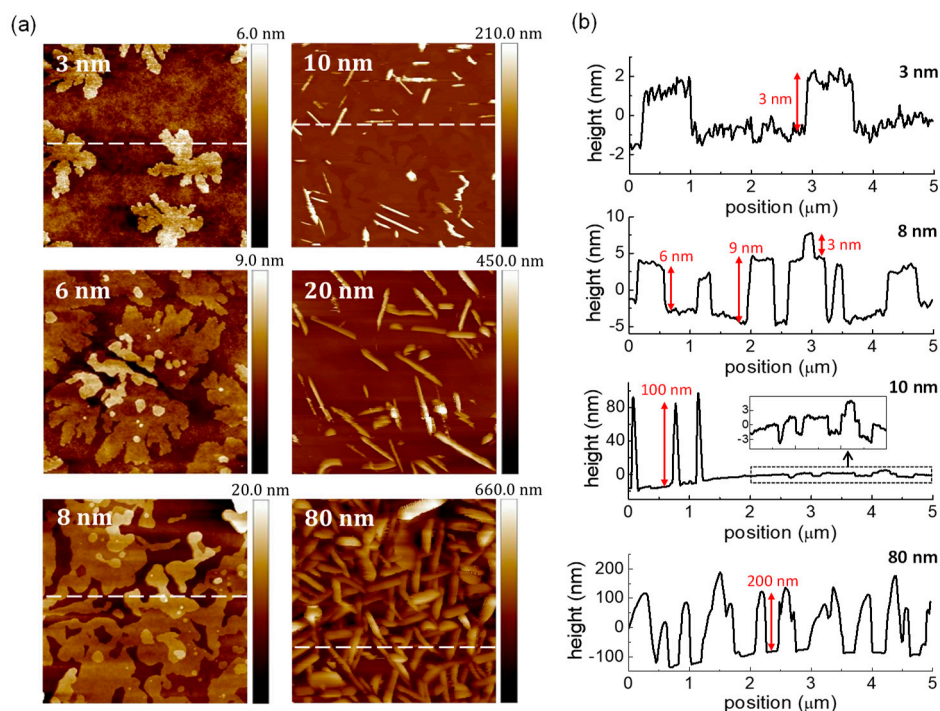
Figure 2. (**a**) Atomic force microscopy (AFM) topographical images (5 μm × 5 μm) of DFH-4T films with different thicknesses deposited on PMMA dielectric and (**b**) height profile cross section for a few selected thicknesses, indicating the formation of multilayered terrace structure below 10 nm and large rod like crystals above 10 nm. The height of each layer in the terrace structure is measured to be ~3 nm. On the other hand, the height and diameter of rod like crystals tend to increase with thickness, from ~100 nm in the 10 nm film to ~200 nm in the 80 nm film.

To assess the crystallinity of the DFH-4T films, synchrotron based XRD diffraction patterns were obtained and presented in Figure 3. DFH-4T in an all-trans configuration has a long molecular dimension of about 30 Å. For the 8 nm thick film, a set of (h00) diffraction peaks already emerge but weaker in intensity due to the presence of only a few repeated molecular units along surface normal direction. As the thickness of the film is increased, the diffraction peaks gain in intensity, as expected. For the thickest film of 80 nm, the most intense (400) peak appears at 5.80° and is accompanied by (600) peak at 8.78° as well as some even weaker but discernible high-order diffraction peaks. Diffraction order was assigned by consulting with earlier published paper [18], in which the large unit cell (a = 61.095 Å, b = 5.750 Å, c = 8.974 Å; $\alpha = \gamma = 90°$, $\beta = 94.5°$) contains four DFH-4T molecules with two DFH-4T arranged along a-axis direction. The fact that the observed diffraction peaks are mostly of (h00) type indicates that the DFH-4T crystallites are formed with their b,c axes of the unit cell in parallel with the substrate surface, resulting in a large d_{200} spacing calculated to be 60.91 Å. Thus, the DFH-4T molecules for the as-arranged crystallites tend to have their long molecular axes aligned perpendicular to the substrate, with in-plane π-π stacking favorable for charge transport. The slight discrepancy in diffraction peak position found between the thin and thick films suggests the presence of structural strain in the thin films. Overall, the thicker films have a higher degree of microstructural order and a smaller interlayer spacing. It is also noted that as the films become thicker with the formation of rod like crystals (>10 nm), new diffraction peaks emerge at higher angles, 11$\bar{1}$) at 18.44° and a smaller one (311) at 19.03°, indicating the presence of some other differently oriented crystallites in the rod like structure. Unlike (h00) crystallites, (311) and (11$\bar{1}$) crystallites tend to have their long molecular axes aligned parallel to the substrate, which may hinder the charge transport to some extent. Probably, the surface roughness of rod-like crystals and their staking geometry may not be able to support a uniform growth of DFH-4T crystallites.
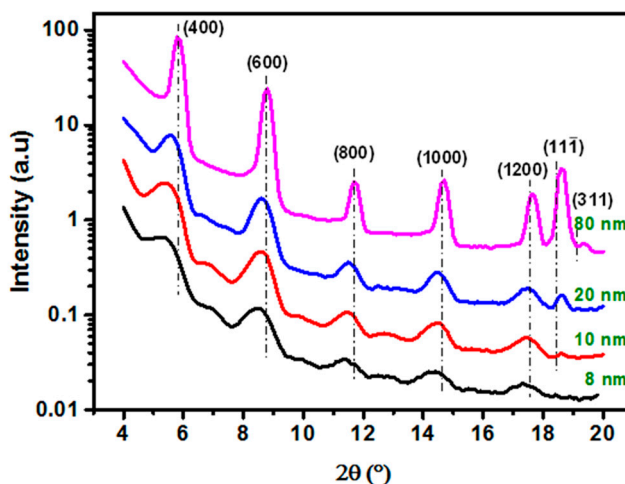
Figure 3. The θ–2θ diffraction patterns obtained with X-ray with an energy of 8.0 keV (λ = 1.5498 Å) for the DFH-4T films of different thickness deposited on PMMA dielectric. The intensity scale is given in a logarithmic scale to highlight the pattern development with thickness. The assignment of diffraction order is consistent with the structure data reported in Ref. [18]. The expected diffraction angles were marked with dash-dot lines.

As XRD is sensitive to the long-range structural ordering of materials but provides very little information about non-crystalline or amorphous part of materials, we thus use a somewhat complementary technique, namely NEXAFS, to reveal the orientation of the molecular constituents of organic materials, irrespective of whether a long-range structural ordering exists. Specifically, by exploring the polarization dependence of NEXAFS π-resonance signal, one can learn how the quarterthiophene units of DFH-4T molecules orient themselves on the surface. This piece of information is important because the degree of resultant π−π overlap greatly influences the charge transport in OFET. The measurements were carried out in a UHV surface science endstation located at the beamline BL24A of Taiwan Light Source (TLS) of NSRRC. NEXAFS data were acquired by means of a homemade partial electron yield (PEY) detector comprising a set of retarding meshes in conjunction with an electron amplification device of microchannel plate. For carbon K-edge spectral acquisition, the retarding voltage was set at −150 V to retard all but the signals derived from carbon Auger decay process for an enhanced signal to background ratio. Figure 4a shows the relevant angular coordinates in measurements, where the soft X-ray with polarization factor (P) determined to be 0.85 for ~300 eV photons is incident at an angle of θ from the sample surface plane. The NEXAFS spectra were then obtained at various values of θ to obtain the angular dependence of the X-ray absorbance. Figure 4b,c show a set of edge-jump normalized carbon K-edge NEXAFS spectra taken at different X-ray incident angles for the 8 nm and 80 nm DFH-4T films grown on PMMA/SiO$_2$. The first major X-ray absorption feature before 286.3 eV is attributed to the 1s-π* resonance and the second absorption feature (286.3 eV to 288.0 eV) is derived from a mixed σ∗ resonances of C-H and C-S types [19,20]. The third absorption feature at 288.5 eV is due to the π* (C=O) resonance of PMMA [21] and becomes much reduced in intensity for 80 nm thick DFH-4T film. The observation of C=O resonance indicates an incomplete covering of PMMA by DFH-4T because otherwise no PMMA signal is expected given a NEXAFS probing depth of 6 nm for the present PEY detection with 150 V retardation voltage [22]. The introduction of two perfluorinated side chains in DFH-4T changes the usual featureless σ* resonance starting from ~290 eV into pronounced peaks. Previous NEXAFS study of oriented perfluoroeicosane (CF$_3$(CF$_2$)$_{18}$CF$_3$) film showed that the absorption onset was shifted from ~284 eV to 290 eV due to the strong chemical shift induced by C–F bond and three prominent σ* resonances of C–C and C–F types appear between 290 eV and 305 eV [23]. Based on this work, the three major features in our spectra are assigned as follows: σ* (C–F) at 292.6 eV, σ* (C–C) at 295.3 eV, and σ* (C–F) at 298.7 eV. We believe that the most reliable way of determining the tilt angle of DFH-4T is to evaluate the X-ray

incidence angle dependence of the fitted intensity of low-energy 1s-π* resonances located between 282.5 eV and 286.25 eV (inset of Figure 4b,c). In this energy window, neither PMMA underlayer nor the perfluorinated side chains contributes any absorption signal and the signal itself is derived from the coplanar quarterthiophene exclusively, which greatly simplifies the data interpretation. The next high-lying absorption feature originated from C–H and C–S resonances has a less clear polarization dependence because of mutually orthogonal σ- and π-polarization dependence from the carbons of thiophenes [20,24]. The analysis based on C–F and C–C σ* resonances is seemingly appealing; however, the presence of step edge and the angle-independent background can make a reliable analysis difficult unless a more complete set of data is available [25].
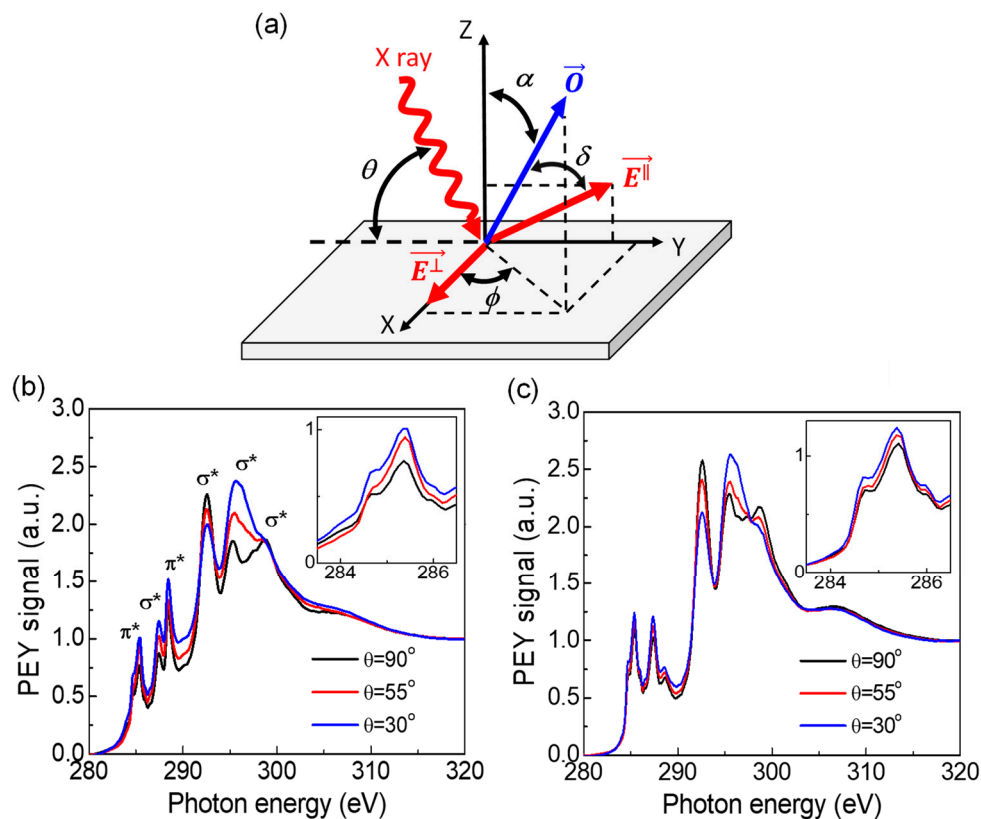

Figure 4. (**a**) Configuration of NEXAFS measurements. X-ray is incident in the *yz* plane and at an angle θ from the surface. The major electric field component $E^{\parallel}$ lies in the storage ring plane *yz* and the minor electric field component $E^{\perp}$ is in *xz* plane. Transitional dipole moment vector $\vec{O}$ is inclined at an angle α from the surface normal direction (*z*) and this inclination angle is determined with NEXAFS. In comparison, the azimuthal angle ϕ cannot be determined in most cases due to the coexistence of multiple surface domains that results in azimuthal averaging. (**b**) and (**c**) show the N K-edge partial electron yield (PEY) data for the 8 nm and 80 nm films deposited on PMMA dielectric, respectively. Scans were taken with the X-ray incident angles at θ = 30°, 55°, 90° measured from surface plane. The inset shows the enlarged plot of the first absorption feature before 286.3 eV, which is attributed to the 1s-π* resonance.

With this in mind, we carried out a complete fitting at the angular dependence of the 1s-π* resonance intensity, as shown in Supplementary Materials Figure S1. The method of estimating the tilt of aromatic ring plane based on crystallographic data was presented in the previous NEXAFS investigation of organic semiconducting film of anthradithiophene derivative [26]. For the 8 nm film, the normalized intensity values are 0.915/1.00/1.18 for 90°/55°/30° incidence angle, which gives a transition dipole momentum vector (perpendicular to thiophene ring plane) at ~50° from the surface normal. That is, the thiophene ring plane is at ~40° from the surface normal. For the 80 nm film,

the normalized intensity values are 0.964/1.00/1.07 for 90°/55°/30° incident angle, indicating that the thiophene ring plane is tilted toward the surface normal by another ~2°. Interestingly, probing of the 8 nm and 80 nm films with drastically different surface morphologies (terrace vs rod like crystals) shows very similar molecular inclinations. It is noted that an averaged ~40° tilt is larger than the molecular inclination deduced from the dominant (*h*00) diffraction in the X-ray data, where the aromatic ring plane is estimated to be inclined from the surface normal by 30° (Figure S2). This discrepancy may arise from a fact that the XRD data are derived solely from the crystalline part of the materials while the NEXAFS data are contributed from *all* the molecules, setting a basis for the data difference. Nonetheless, the NEXAFS data are consistent with the X-ray result that DFH-4T mainly adopts an edge-on molecular orientation. From these two techniques, it can be claimed that the DFH-4T films are constituted mainly with (*h*00) crystallites but also with some differently oriented crystallites and amorphous components, however, the overall crystallite structure and molecular orientation do not show much difference with respect to film thickness increase.

4. Temperature Dependent Transport Measurement and Analysis

Next, we conduct the low temperature measurement to investigate the electronic states and transport properties of DFH-4T transistors with various thicknesses. Figure 5a–d show the linear transfer characteristics (V_d = 10 V) of DFH-4T transistors over a temperature range from 300 K to 100 K for different thicknesses from 8 nm to 80 nm, plotted on both a logarithmic and a linear scale. As the temperature decreases, all the devices exhibit a decrease of on-current and a positive shift of V_{on}, indicating an increased trapping of immobile charges in the deep localized states. V_{th} is shifted to more positive values at lower temperature for the thicknesses of 8–10 nm and tends to be independent of temperature for the thicknesses of >10 nm. To compare these devices with different temperature dependences of V_{th}, we include the threshold voltage effect into calculation of the gate dependent mobility by taking transconductance ($\partial I_d/\partial V_g$) of the transfer curves in the linear regime [27]

$$\mu_{lin}(V_g,\ T) = \frac{L}{WC_iV_d}\left(\frac{\partial I_d}{\partial V_g}\right)_{V_g-V_{th}\gg V_d} \tag{2}$$

with the fixed V_g–V_{th} for all the temperatures. In this way the amount of accumulated charges in the channel is determined only by the values of V_g–V_{th} and is independent of temperature. Figure 5e–h show the temperature dependence of linear mobilities extracted for different transistors. In the linear regime, the choice of V_g–V_{th} values needs to be sufficiently large as compared to V_d. Note that this condition is not well satisfied for the 8 nm device, since its relatively high V_{th} at low temperature limits the maximum value of V_g–V_{th} in the gate sweep range to be only slightly larger than V_d. Nevertheless, because the transconductance of the 8 nm device is weakly dependent on V_g above V_{th}, the extracted mobility could be similar to but only slightly lower than that if extracted with larger V_g–V_{th} and is still valid for further analysis. For all the devices, it can be seen that the temperature dependent mobility is nonmonotonic. Below 240 K the mobilities approximately follow the Arrhenius rule. The activation energy extracted from 80–240 K is 23.4 meV for 8 nm device and reduces to 8.3 meV for 80 nm device. Above 240 K the mobilities increase with temperature in a steeper slope compared to the lower temperature regime. Such a change of slope at elevated temperature has also been observed in some microcrystalline organic semiconductors and been interpreted as due to a nonzero band-tail mobility in the mobility-edge (ME) model [28]. From the low activation energy extracted below 240 K, we speculate that the DFH-4T films have a relatively narrow distribution of trap states. Therefore, in addition to being thermally activated, small amounts of charge could tunnel through the trap states and lead to the increased slope. For simplicity, we mainly analyze the low temperature regime (80–240 K) with the ME model, where the mobility in the band-tail states can be reasonably assumed to be zero.
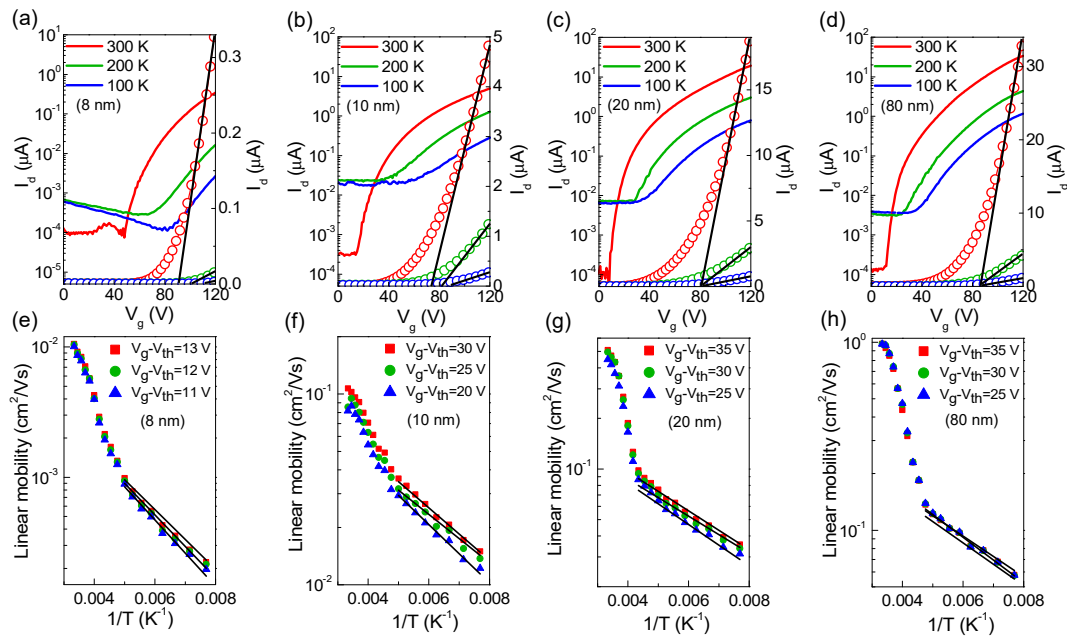
Figure 5. (**a**–**d**) Temperature dependence of the linear transfer characteristics (V_d = 10 V) of the DFH-4T transistors with various thicknesses, plotted on a logarithmic scale and a linear scale (open circles). The black lines provide a visual guide to the values of V_{th} for the different temperatures. For the transistors with thicknesses of 8–10 nm, V_{th} shifts to larger value as temperature decreases but remains the same for the greater thickness of 20–80 nm. (**e**–**h**) Temperature dependence of the linear mobilities of the DFH-4T transistors extracted from the transfer characteristics as shown in (**a**–**d**) for various thicknesses (solid dots) and the effective mobilities calculated by using the ME model (lines) are shown for comparison.

The ME model assumes that the mobile and localized states of a semiconductor are separated by a defined energy, that is, the mobility edge and carriers are transported in the mobile states with a constant mobility (μ_i) and trapped in the localized states with zero mobility. According to Ref. [29], we define the mobility edge as E = 0 eV. The localized states (E > 0) are described with an exponential density of states (DOS) that decay in the band gap,

$$D_{tail}(E) = \frac{N_{tail}}{w_{tail}} \exp\left(-\frac{E}{w_{tail}}\right), \tag{3}$$

where N_{tail} represents the concentration of band-tail states and w_{tail} is the width of exponential trap distribution. On the other hand, the mobile states (E < 0) are described based on a simple form for 3-D free electron gas (D(E)~$E^{1/2}$ [30]):

$$D_{mob}(E) = \frac{N_{tail}}{w_{tail}} \sqrt{\frac{E_c - E}{E_c}}, \tag{4}$$

where E_c is a free parameter used to tailor the shape of DOS in the mobile states. Since the variation of E_c is insensitive to the fitting result of mobilities [31], we fix E_c = 30 meV in this work. When the gate bias is applied, the total accumulated charge concentration (N_{tot}) would equal to the summation of the charge concentrations in the mobile states and in the localized states:

$$N_{tot} = \frac{C_i|V_g - V_{th}|}{h} = \int_{-\infty}^{0} D_{mob}(E)f(E_F, E)dE + \int_{0}^{\infty} D_{tail}(E)f(E_F, E)dE, \tag{5}$$

where h = 1×10^{-7} cm is the channel dimension normal to the dielectric surface and $f(E_F, E)$ is the Fermi-Dirac distribution of electrons. After solving the Fermi energy $E_F(V_g, T)$ in Equation (5), the charge concentrations in the mobile states

$$N_{mob} = \int_{-\infty}^{0} D_{mob}(E) f(E_F, E) dE \tag{6}$$

can be calculated and then the effective mobility can be determined by the fraction of mobile charges,

$$\mu(V_g, T) = \mu_i \frac{N_{mob}(V_g, T)}{N_{tot}}. \tag{7}$$

In Figure 5e–h we show the best fit to the temperature dependent mobility at different $V_g - V_{th}$ values for all the devices by using Equation (7) with μ_i, N_{tail} and w_{tail} as free parameters. The values of the fitting parameters are given in Table 1. Overall, the transistors with thicker DFH-4T have higher intrinsic mobilities μ_i and narrower bandwidths w_{tail} and lower concentrations N_{tail} of localized states. From the above structural characterizations, it is not surprising that a high population of film voids, discontinuities and a high degree of microstructural disorder in the 8 nm device result in a high energetic disorder and hence the largest N_{tail} and w_{tail}. On the other hand, the intrinsic mobility reflects the degree of polaron delocalization in the mobile states [28]. The poorer crystallinity of the 8 nm device may lead to an increased localization of the polaron wave function in the crystalline domains, which accounts for a low band mobility. As the film grows thicker, the film continuity and crystallinity are improved, so that the energetic disorder decreases, and intrinsic mobility increases. Importantly, the ME model predicts that the increase in μ_i and decrease in w_{tail} and N_{tail} are most pronounced for the thickness of 8-10 nm but not obvious for the thickness exceeding 20 nm. This result provides unambiguous evidence that the electronic state of DFH-4T transistors is mainly related to the structural properties of bottom terrace but is weakly related to the conformation of top rod like crystals. Therefore, we can confirm that the conductive channel is located at the bottom terrace, consistent with the general expectation that gate-induced charge accumulation occurs within a few nanometers from the dielectric/semiconductor interface. The high mobility thus relies primarily on reduction of trap states by improving film continuity and crystalline quality of the terrace structure.

Table 1. Parameters extracted from fitting the experimental data to the ME model.

Thickness (nm)	μ_i (cm$^2 \cdot$V$^{-1} \cdot$s^{-1})	w_{tail} (meV)	N_{tail} (cm^{-3})
8	0.0063	20	5.3×10^{19}
10	0.11	16	4.8×10^{19}
20	0.207	14.8	4.7×10^{19}
80	0.34	14.3	4.3×10^{19}

5. Morphological Effect on Charge Injection

Although the conformation of top rod like crystals is shown to be little correlated with the charge transport, how these crystals influence the charge injection from the top electrodes remains a question. To evaluate this effect on the transistor performance, we measure the low-frequency C–V response of the metal-insulator-semiconductor (MIS) diodes (Si/SiO$_2$/PMMA/DFH-4T/Ag) of varied DFH-4T thickness. The metal-insulator-metal (MIM) diodes (Si/SiO$_2$/PMMA/Ag) were also measured as a control. In the MIS diodes the DFH-4T and top Ag electrode were sequentially evaporated through a fixed shadow mask to eliminate the parasitic capacitance. The same shadow mask was also used to define the top contact of the MIM diode. The C–V measurements were performed using a 4192 A Hewlett Packard Impedance analyzer in a nitrogen glove box. Since the maximum output voltage of impedance analyzer is limited at 35 V, we fabricated the MIS and MIM diodes with the thinner dielectrics (70 nm SiO$_2$ and 90 nm PMMA) to yield the dielectric capacitance (19.4 nF·cm^{-2}) about

three times higher than that of transistors (6.4 nF·cm^{-2}). In this way, a complete switch-on behavior of the MIS diodes can be obtained with an applied voltage of 35 V, which corresponds to that of transistors as driven with V_g ~ 100 V.

Typically, for a planar MIS diode, the capacitance has the lowest value in depletion and starts to increase with V_g above the threshold as the accumulated charges move closer to the semiconductor/insulator interface and saturates at the value approaching the insulator capacitance in the high V_g regime. That is, the C–V response also indicates how the resistance (including contact and semiconductor bulk) varies with V_g. As the result shown in Figure 6a, all the DFH-4T MIS diodes exhibit the C–V response in a similar manner as expected for typical planar diodes but the values of capacitance in depletion and accumulation regimes strongly depend on the thickness. In depletion regime the capacitance decreases as the thickness increases, which is as expected because the thicker DFH-4T film has a lower capacitance and hence a lower serial capacitance of the insulator and semiconductor capacitors. The charge injection in different MIS diodes manifests itself more clearly in accumulation regime. Opposite to the trend in depletion regime, the capacitance is found to increase with the thickness in accumulation regime. In the 8 nm diode, the capacitance saturates at a relatively low value compared to the insulator capacitance measured from the MIM diode (C_{in}), indicating the presence of a portion of nonconductive region due to a high population of structural defects in the multilayered terrace. The capacitance of the 10 nm diode saturates at a higher value and approaches that of MIM diode, suggesting an improved structural quality. Interestingly, the capacitance of the 20 nm diode exceeds that of MIM diode in the high V_g regime. This may be resulted from two phenomena: First, the nonconductive defects almost diminish in the multilayered terrace at the thickness between 10 nm and 20 nm, as evidenced by the AFM measurement (see Figure 2). Second, the topography of top rod like crystals in the 20 nm DFH-4T could be sufficiently rough, so that the effective contact area (A_{eff}) of DFH-4T/metal interface is apparently larger than the contact area (A_{in}) of MIM diode, resulting in a higher effective capacitance $C_{eff} = C_{in}A_{eff}/A_{in}$ [16]. In the 80 nm diode, the capacitance undergoes an obvious "two-stage" increase from the lowest value in depletion regime to the highest value in accumulation regime, suggesting a nonmonotonic charge accumulation process. As illustrated in Figure 6b, in the first stage (low positive V) the injected charges fill the crystal boundary defect states and disorder sites within the crystals, forming conducting pathways between the top contacts and the bottom terrace. Increase in V_g allows injection of more charges and leads to the formation of more conducting pathways and enhances conductivity of crystal network, so that the capacitance increases accordingly. In this stage, only the top crystal network becomes conducting whereas the bottom terrace remains insulating. The inflection point between the first and second stages (capacitance approaching that of thinner MIS diodes in depletion regime, ~18.8 nF·cm^{-2}) occurs when the charges start to be accumulated in the bottom terrace, which corresponds to the effective turn-on threshold of transistor characteristic. In the second stage (high positive V), the capacitance continuously increases with V_g and reaches an even higher value than that of the 20 nm diode without apparent saturation. Again, this can be interpreted with the topography of top rod like crystals in the 80 nm DFH-4T. Due to a very large A_{eff} of DFH-4T/metal interface in the crystal network, injection of more charges with higher V_g produces even more available conducting pathways. Therefore, not only the conductivity of the crystal network continuously increases but more charges can be accumulated in the bottom terrace, which together leads to an unsaturated and a very high C_{eff} in the high V_g regime. Overall, the C–V measurement provides a clear insight of how the conformation of top crystals affects charge injection and accumulation in the DFH-4T transistors. The thicker films with more densely packed crystals on one hand have more defect states that need to be filled before effective accumulation takes place in the bottom terrace, while on the other hand can produce a larger A_{eff} of DFH-4T/metal interface that allows injection of more charges to contribute a higher current. This well explains why the transistors with >10 nm DFH-4T exhibit an unexpectedly increased V_{th} (Figure 1c) but also a sharply increased on-current, which is particularly evident in the 80 nm device. Such a morphological effect on charge injection/accumulation processes should also be taken into account in some small

molecule devices with similar large crystal growth at sufficiently large thicknesses [32]. We speculate that the formation of rod like crystals in the DFH-4T films of >10 nm might be resulted from several mechanisms. First, a small amount of aggregates formed in the first few layers of terrace structure serve as the seeds to initiate the crystal growth. Second, due to the high electronegativity of fluorinated side chains, the dipole-dipole interaction between molecules could be so strong to hold molecules together, resulting in a rapid growth of large crystals into three dimensions. Third, the π-stacking interaction between thiophene rings may favor elongation of crystals in in-plane direction. By developing novel deposition approaches capable of controlling various factors on the crystal growth, it is possible to minimize the crystal defects and maximize the contact area with the top electrodes, so that V_{th} can be further reduced while achieving a higher on-current.
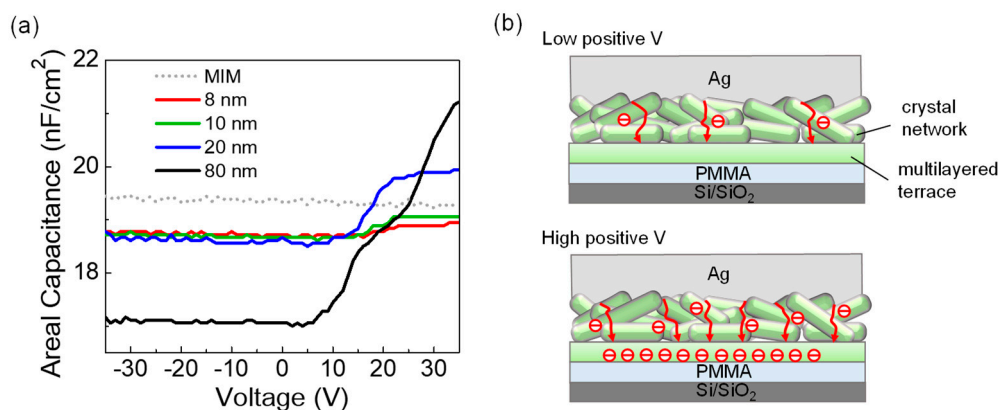

Figure 6. (**a**) Capacitance-voltage curves of the DFH-4T MIS diodes with various DFH-4T thicknesses and the metal-insulator-metal (MIM) diode. (**b**) Illustration showing the electron injection and accumulation at low and high positive applied voltage in the 80 nm DFH-4T MIS diode with the film thickness not shown to scale.

6. Conclusions

We present a detailed study of the correlation between the electronic and structural properties of the DFH-4T transistors as controlled by film thickness. The transistor characterizations show that the field-effect mobility becomes observable in the film of 8 nm, then increases sharply from 8 nm to 10–20 nm and levels off above 20 nm. The threshold voltage first decreases from 8 nm to 10 nm, then increases with thickness above 10 nm. Such variations in the mobility and threshold voltage are closely correlated with the structural evolution in the film growth. The morphology characterizations show that DFH-4T films evolve form multilayered terrace structure for the first 10–20 nm to a structure dominated with randomly distributed rod like crystals at larger film thickness. Despite this drastic change in the morphology, the molecules of the films exhibit similar orientation but are packed into the crystallites of improved ordering for the thicker films. Low temperature transport analyses further demonstrate that the electronic state and transport property of DFH-4T transistors are determined by the bottom terrace structure. The significantly improved film continuity and crystalline quality of the bottom terrace as the thickness increases from 8 nm to 20 nm result in an apparently reduced bandwidth of shallow trap states and enhanced intrinsic mobilities, which accounts for the sharply increased mobility. On the other hand, the rod like crystals appearing above 10 nm are shown to weakly affect the transport property in the channel region but have a direct impact on the charge injection and accumulation process. The C–V measurements of the DFH-4T MIS diodes clearly suggest that a higher density of rod like crystals in a thicker film has more defects in the crystal regions but also produces a larger effective DFH-4T/metal contact area for charge injection. This explains an increased threshold voltage, but higher on-current levels achieved in the transistors with thickness exceeding 10 nm. Put it all together, our study affords a better understanding of the structural factors that govern charge transport and injection in DFH-4T transistors with complex film morphology.

When processing DFH-4T films for various device applications, it is not only important to optimize the structural order of bottom terrace to achieve high electron mobilities but also necessary to control the growth of top crystals that may impose strong morphological effects on subsequently deposited metals or semiconductors and affect the overall charge injection/accumulation properties in the devices.

Supplementary Materials: The following are available online at http://www.mdpi.com/2073-4352/9/3/144/s1, Figure S1: The fitting of NEXAFS spectrum, Figure S2: Molecular constituents of (*h*00)-aligned DFH-4T crystallites.

Author Contributions: J.-F.C. designed the experiments and wrote the main text of the manuscript. H.-S.S. fabricated the devices and conducted AFM, temperature dependent transport and C–V measurements. Y.-W.Y. and C.-H.W. contributed to the X-ray diffraction and NEXAFS measurements and data interpretation.

Conflicts of Interest: The authors declare no conflict of interest.

References

1. Usta, H.; Facchetti, A.; Marks, T.J. n-Channel semiconductor materials design for organic complementary circuits. *Acc. Chem. Res.* **2011**, *44*, 501–510. [CrossRef]
2. Muccini, M. A bright future for organic field-effect transistors. *Nat. Mater.* **2006**, *5*, 605–613. [CrossRef]
3. Usta, H.; Sheets, W.C.; Denti, M.; Generali, G.; Capelli, R.; Lu, S.; Yu, X.; Muccini, M.; Facchetti, A. Perfluoroalkyl-functionalized thiazole–thiophene oligomers as n-channel semiconductors in organic field-effect and light-emitting transistors. *Chem. Mater.* **2014**, *26*, 6542–6556. [CrossRef]
4. de Zerio Mendaza, A.D.; Melianas, A.; Rossbauer, S.; Bäcke, O.; Nordstierna, L.; Erhart, P.; Olsson, E.; Anthopoulos, T.D.; Inganäs, O.; Müller, C. High-entropy mixtures of pristine fullerenes for solution-processed transistors and solar cells. *Adv. Mater.* **2015**, *27*, 7325–7331. [CrossRef]
5. Zhao, X.; Liu, T.; Cui, Y.; Hou, X.; Liu, Z.; Dai, X.; Kong, J.; Shi, W.; Dennis, T.J.S. Antisolvent-assisted controllable growth of fullerene single crystal microwires for organic field effect transistors and photodetectors. *Nanoscale* **2018**, *10*, 8170–8179. [CrossRef] [PubMed]
6. Zhang, F.; Hu, Y.; Schuettfort, T.; Di, C.-A.; Gao, X.; McNeill, C.R.; Thomsen, L.; Mannsfeld, S.C.B.; Yuan, W.; Sirringhaus, H.; et al. Critical role of alkyl chain branching of organic semiconductors in enabling solution-processed n-channel organic thin-film transistors with mobility of up to 3.50 cm^2 V^{-1} s^{-1}. *J. Am. Chem. Soc.* **2013**, *135*, 2338–2349. [CrossRef] [PubMed]
7. Welford, A.; Maniam, S.; Gann, E.; Thomsen, L.; Langford, S.J.; McNeill, C.R. Thionation of naphthalene diimide molecules: Thin-film microstructure and transistor performance. *Org. Electron.* **2018**, *53*, 287–295. [CrossRef]
8. Tilley, A.J.; Guo, C.; Miltenburg, M.B.; Schon, T.B.; Yan, H.; Li, Y.; Seferos, D.S. Thionation enhances the electron mobility of perylene diimide for high performance n-channel organic field effect transistors. *Adv. Funct. Mater.* **2015**, *25*, 3321–3329. [CrossRef]
9. Xu, X.; Yao, Y.; Shan, B.; Gu, X.; Liu, D.; Liu, J.; Xu, J.; Zhao, N.; Hu, W.; Miao, Q. Electron mobility exceeding 10 cm^2 V^{-1} s^{-1} and band-like charge transport in solution-processed n-channel organic thin-film transistors. *Adv. Mater.* **2016**, *28*, 5276–5283. [CrossRef] [PubMed]
10. Wu, Q.; Ren, S.; Wang, M.; Qiao, X.; Li, H.; Gao, X.; Yang, X.; Zhu, D. Alkyl chain orientations in dicyanomethylene-substituted 2,5-di(thiophen-2-yl)thieno-[3,2-b]thienoquinoid: Impact on solid-state and thin-film transistor performance. *Adv. Funct. Mater.* **2013**, *23*, 2277–2284. [CrossRef]
11. Facchetti, A.; Mushrush, M.; Katz, H.E.; Marks, T.J. n-Type building blocks for organic electronics: A homologous family of fluorocarbon-substituted thiophene oligomers with high carrier mobility. *Adv. Mater.* **2003**, *15*, 33–38. [CrossRef]
12. Facchetti, A.; Mushrush, M.; Yoon, M.-H.; Hutchison, G.R.; Ratner, M.A.; Marks, T.J. Building blocks for n-type molecular and polymeric electronics. Perfluoroalkyl-versus alkyl-functionalized oligothiophenes (nT; *n* = 2–6). Systematics of thin film microstructure, semiconductor performance, and modeling of majority charge injection in field-effect transistors. *J. Am. Chem. Soc.* **2004**, *126*, 13859–13874.

13. Yoon, M.-H.; Kim, C.; Facchetti, A.; Marks, T.J. Gate dielectric chemical structure−organic field-effect transistor performance correlations for electron, hole, and ambipolar organic semiconductors. *J. Am. Chem. Soc.* **2006**, *128*, 12851–12869. [CrossRef] [PubMed]

14. Capelli, R.; Toffanin, S.; Generali, G.; Usta, H.; Facchetti, A.; Muccini, M. Organic light-emitting transistors with an efficiency that outperforms the equivalent light-emitting diodes. *Nat. Mater.* **2010**, *9*, 496–503. [CrossRef] [PubMed]

15. Chang, J.-F.; Chen, W.-R.; Lai, Y.-C.; Chien, F.-C. Red phosphorescent trilayer organic light-emitting field-effect transistors with a wide recombination zone. *Jpn. J. Appl. Phys.* **2016**, *55*, 020304. [CrossRef]

16. Chang, J.-F.; Chen, W.-R.; Huang, S.-M.; Lai, Y.-C.; Lai, X.-Y.; Yang, Y.-W.; Wang, C.-H. High mobility ambipolar organic field-effect transistors with a nonplanar heterojunction structure. *Org. Electron.* **2015**, *27*, 84–91. [CrossRef]

17. Dholakia, G.R.; Meyyappan, M.; Facchetti, A.; Marks, T.J. Monolayer to multilayer nanostructural growth transition in n-type oligothiophenes on Au(111) and implications for organic field-effect transistor performance. *Nano Lett.* **2006**, *6*, 2447–2455. [CrossRef]

18. Facchetti, A.; Yoon, M.-H.; Stern, C.L.; Hutchison, G.R.; Ratner, M.A.; Marks, T.J. Building blocks for n-type molecular and polymeric electronics. Perfluoroalkyl- versus alkyl-functionalized oligothiophenes (nTs; n = 2–6). Systematic synthesis, spectroscopy, electrochemistry, and solid-state organization. *J. Am. Chem. Soc.* **2004**, *126*, 13480–13501. [CrossRef]

19. DeLongchamp, D.M.; Kline, R.J.; Lin, E.K.; Fischer, D.A.; Richter, R.J.; Lucas, L.A.; Heeney, M.; McCulloch, I.; Northrup, J.E. High carrier mobility polythiophene thin films: Structure determination by experiment and theory. *Adv. Mater.* **2007**, *19*, 833–837. [CrossRef]

20. Lue, J.-W.; Lin, Y.-H.; Yang, Y.-W. Growth and electronic structure studies of semiconducting thin films of fluorine-monosubstituted fused-thiophene derivative. *J. Electron Spectrosc. Relat. Phenom.* **2014**, *196*, 49–53. [CrossRef]

21. Dhez, O.; Ade, H.; Urquhart, S.G. Calibrated NEXAFS spectra of some common polymers. *J. Electron Spectrosc. Relat. Phenom.* **2003**, *128*, 85–96. [CrossRef]

22. Zharnikov, M.; Frey, S.; Heister, K.; Grunze, M. An extension of the mean free path approach to X-ray absorption spectroscopy. *J. Electron Spectrosc. Relat. Phenom.* **2002**, *124*, 15–24. [CrossRef]

23. Ohta, T.; Seki, K.; Yokoyama, T.; Morisada, I.; Edamatsu, K. Polarized XANES studies of oriented polyethylene and fluorinated polyethylenes. *Phys. Scr.* **1990**, *41*, 150–153. [CrossRef]

24. Väterlein, P.V.; Fink, R.; Umbach, E.; Wurth, W. Analysis of the x-ray absorption spectra of linear saturated hydrocarbons using the Xα scattered-wave method. *J. Chem. Phys.* **1998**, *108*, 3313–3320. [CrossRef]

25. Stöhr, J. *NEXAFS Spectroscopy*; Springer: Berlin, Germany, 1992.

26. Wang, C.-H.; Cheng, Y.-C.; Su, J.-W.; Fan, L.-J.; Huang, P.-Y.; Chen, M.-C.; Yang, Y.-W. Origin of high field-effect mobility in solvent-vapor annealed anthradithiophene derivative. *Org. Electron.* **2010**, *11*, 1947–1953. [CrossRef]

27. Brown, A.R.; Jarrett, C.P.; deLeeuw, D.M.; Matters, M. Field-effect transistors made from solution-processed organic semiconductors. *Synth. Met.* **1997**, *88*, 37–55. [CrossRef]

28. Street, R.A.; Northrup, J.E.; Salleo, A. Transport in polycrystalline polymer thin-film transistors. *Phys. Rev. B* **2005**, *71*, 165202. [CrossRef]

29. Salleo, A.; Chen, T.W.; Völkel, A.R.; Wu, Y.; Liu, P.; Ong, B.S.; Street, R.A. Intrinsic hole mobility and trapping in a regioregular poly(thiophene). *Phys. Rev. B* **2004**, *70*, 115311. [CrossRef]

30. Street, R.A. *Hydrogenated Amorphous Silicon*; Cambridge University Press: Cambridge, UK, 1991.

31. Chang, J.-F.; Sirringhaus, H.; Giles, M.; Heeney, M.; McCulloch, I. Relative importance of polaron activation and disorder on charge transport in high-mobility conjugated polymer field-effect transistors. *Phys. Rev. B* **2007**, *76*, 205204. [CrossRef]

32. Shi, J.; Wang, H.; Song, D.; Tian, H.; Geng, Y.; Yan, D. n-Channel, ambipolar, and p-channel organic heterojunction transistors fabricated with various film morphologies. *Adv. Funct. Mater.* **2007**, *17*, 397–400. [CrossRef]